

## Article

# Surface-Pore-Modified N-Doped Amorphous Carbon Nanospheres Tailored with Toluene as Anode Materials for Lithium-Ion Batteries

Shiran Shan <sup>1</sup>, Chunze Yuan <sup>1,2,\*</sup> , Guangsu Tan <sup>1</sup>, Chao Xu <sup>1</sup>, Lin Li <sup>1,2</sup> , Guoqi Li <sup>1</sup>, Jihao Zhang <sup>1</sup> and Tsu-Chien Weng <sup>1,2,\*</sup>

<sup>1</sup> School of Physical Science and Technology, ShanghaiTech University, Shanghai 201210, China; shanshr@shanghaitech.edu.cn (S.S.); tangs@shanghaitech.edu.cn (G.T.); xuchao1@shanghaitech.edu.cn (C.X.); lilin1@shanghaitech.edu.cn (L.L.); ligq1@shanghaitech.edu.cn (G.L.); zhangjh5@shanghaitech.edu.cn (J.Z.)  
<sup>2</sup> Center for Transformative Science, ShanghaiTech University, Shanghai 201210, China  
\* Correspondence: yuanchz@shanghaitech.edu.cn (C.Y.); wengzq@shanghaitech.edu.cn (T.-C.W.)

**Abstract:** The surface modification of amorphous carbon nanospheres (ACNs) through templates has attracted great attention due to its great success in improving the electrochemical properties of lithium storage materials. Herein, a safe methodology with toluene as a soft template is employed to tailor the nanostructure, resulting in ACNs with tunable surface pores. Extensive characterizations through transmission electron microscopy (TEM), scanning electron microscopy (SEM), Raman spectroscopy, X-ray diffraction (XRD), X-ray photoelectron spectroscopy (XPS), and nitrogen adsorption/desorption isotherms elucidate the impact of surface pore modifications on the external structure, morphology, and surface area. Electrochemical assessments reveal the enhanced performance of the surface-pore-modified carbon nanospheres, particularly ACNs-100 synthesized with the addition of 100  $\mu\text{L}$  toluene, in terms of the initial discharge capacity, rate performance, and cycling stability. The interesting phenomenon of persistent capacity increase is ascribed to lithium ion movement within the graphite-like interlayer, resulting in ACNs-100 experiencing a capacity upswing from an initial 320  $\text{mAh g}^{-1}$  to a zenith of 655  $\text{mAh g}^{-1}$  over a thousand cycles at a rate of 2 C. The findings in this study highlight the pivotal role of tailored nanostructure engineering in optimizing energy storage materials.

**Keywords:** lithium-ion battery; amorphous carbon nanospheres; anode; soft template



**Citation:** Shan, S.; Yuan, C.; Tan, G.; Xu, C.; Li, L.; Li, G.; Zhang, J.; Weng, T.-C. Surface-Pore-Modified N-Doped Amorphous Carbon Nanospheres Tailored with Toluene as Anode Materials for Lithium-Ion Batteries. *Nanomaterials* **2024**, *14*, 772. <https://doi.org/10.3390/nano14090772>

Academic Editor: Carlos Miguel Costa

Received: 7 March 2024

Revised: 29 March 2024

Accepted: 5 April 2024

Published: 28 April 2024



**Copyright:** © 2024 by the authors. Licensee MDPI, Basel, Switzerland. This article is an open access article distributed under the terms and conditions of the Creative Commons Attribution (CC BY) license (<https://creativecommons.org/licenses/by/4.0/>).

## 1. Introduction

Due to their high energy density, high coulombic efficiency, and long cycle life [1–4], rechargeable lithium-ion batteries (LIBs) are favored for the widespread use of everyday electronic devices and electric vehicles [3]. The anode material as an important component of LIBs, playing an important role in their safety, capacity, and cycle life. Graphite is a very common commercial anode material for LIB; however, its theoretical capacity is limited to only 372  $\text{mAh g}^{-1}$  and has a poor rate capability [5]. This limitation hinders the battery's overall performance, making it insufficient to keep up with the growing demands of the electronics market.

A great deal of effort has been devoted to the exploration of alternative anode materials with improved capacity and rate performance to replace graphite [6–13]. Due to their wide range of sources, tunable ability, strong structure, short diffusion path, etc., nanostructured carbon materials were considered to be a superior choice for future high-performance LIBs [14–20]. Extensive research has been conducted on a variety of nanostructured carbon materials as potential anode materials for LIBs, including graphene [13,18,21], carbon nanospheres [15], carbon nanotubes [19], carbon fibers [16], and carbon quantum dots [22]. Among them, carbon nanospheres have received a lot of attention due to their large specific surface area and ease of tuning and decorating, which can increase their contact area

with the electrolyte and shorten the diffusion path for lithium ions [23]. Additionally, its robust internal structure ensures higher stability, to improve the cycle stability and rate performance of LIBs, thus providing long-term cycle use and fast charging performance in practical applications [2].

To shorten the diffusion path of mass transfer, substantial research efforts have focused on the design and manipulation of carbon nanospheres, achieved by reducing the diameter of carbon spheres to the nanometer scale, thereby enhancing the abundance of exposed surface active sites [23–25]. For instance, researchers have synthesized carbon spheres with a diameter of about 200 nm, yielding a specific capacity of 378 mAh g<sup>-1</sup> at a rate of 0.1 C [24]. Furthermore, an alternative approach has involved the utilization of templates to regulate the surface of carbon nanospheres, resulting in a larger specific surface area, shorter transfer path, and large pore volume. For example, SiO<sub>2</sub> served as a hard template for the surface modification of carbon spheres, yielding a maximum specific surface area of 1117 m<sup>2</sup> g<sup>-1</sup> and a pore volume of 1.77 cm<sup>3</sup> g<sup>-1</sup> [26]. However, the use of HF to remove SiO<sub>2</sub> undoubtedly increases the safety risk of the overall synthesis procedure. In another study, mesoporous carbon nanospheres featuring surface pores showed an enhanced specific capacity of 560 mAh g<sup>-1</sup> at a rate of 0.1 C, approximately twice that of unmodified carbon nanospheres, and exhibited a high capacity of 240 mAh g<sup>-1</sup> at an increased rate of 5 C [27]. In addition, by introducing single or double heteroatoms (boron, nitrogen, sulfur, oxygen, and phosphorus) into the carbon skeleton, the electronic and chemical structure can be adjusted, which can improve the electronic conductivity, expand the interlayer distance, improve the absorption of Li<sup>+</sup> / electrolyte, and provide more active sites to improve the storage and recycling performance of Li [28–30]. Nitrogen (N) atoms have a high electronegativity and atomic diameter, similar to carbon, and are the most widely used heteroatoms, being able to provide free electrons to the  $\pi$  system of carbon to improve its conductivity [31] and introduce active sites to improve the electrochemical reaction performance and obtain a higher lithium ion storage capacity [32]. For example, Wang et al. [29,30] demonstrated that the specific capacity can be increased to 600 mAh g<sup>-1</sup> when 3.9% N is doped in a graphitic carbon framework. The calculation results showed that additional Li storage capacity (higher than 395.21 mAh g<sup>-1</sup>) can be generated at the nanopore and N-doped edges due to the presence of pyridine and pyrrole nitrogen as active sites for the adsorption of Li atoms.

In this study, we presented a safe and conventional synthesis route of amorphous carbon nanospheres (ACNs) and investigated the influence of their surface morphology on lithium storage when used as an anode material. For safe synthesis, toluene served as a soft template to control the surface morphology of the ACNs. Four ACN samples, each featuring distinct surface pore sizes, were prepared by adjusting the amount of toluene during synthesis. The synthesized ACNs were characterized by transmission electron microscopy (TEM), scanning electron microscopy (SEM), Raman spectroscopy, X-ray diffraction (XRD), X-ray photoelectron spectroscopy (XPS), and nitrogen adsorption/desorption isotherms. The ACNs assembled as lithium-ion battery anodes exhibited a significantly enhanced electrochemical performance when using surface-pore-modified nanospheres compared to the unmodified nanospheres. The modified nanospheres demonstrated a remarkable reversible capacity of up to ~600 mAh g<sup>-1</sup> at a rate of 0.05 C. In cycling stability tests at a rate of 2 C, all the ACN samples displayed capacity increases with cycling over 1000 cycles. Notably, the best-performing sample, ACNs-100 (with 100  $\mu$ L toluene added in synthesis), demonstrated an increase in capacity from an initial 320 to a peak of 655 mAh g<sup>-1</sup> in 1100 cycles.

## 2. Experimental Procedures

### 2.1. Materials

Triblock poly(ethylene oxide)-b-poly(propylene oxide)-b-poly(ethylene oxide) Pluronic F-127 (PEO106PPO70PEO106, Mw = 12,600 g mol<sup>-1</sup>) was obtained from Sigma-Aldrich (Shanghai, China). Ammonium persulfate was purchased from Maclin (Shanghai, China).

1,3,5-Tris(4-aminophenyl) benzene (TAPB) was purchased from Adamas (Shanghai, China). Anhydrous ethanol, hydrochloric acid, and toluene were obtained from Sinopharm Chemical Reagent Co., Ltd. (Shanghai, China). All chemicals were of analytical grade and used without further purification. Deionized water was taken from a YISHUO Purification system (Shanghai, China) for all experiments.

### 2.2. Preparation of N-Doped Amorphous Carbon Nanospheres (ACNs)

N-doped ACNs were prepared by using TAPB as a nitrogen and carbon source, Pluronic F-127 as surfactant, and ethanol and water as organic cosolvent agent, followed by catalytic polymerization and carbonization. In a classic synthesis, 0.1 g Pluronic F-127 and 100  $\mu\text{L}$  of toluene were dispersed in 6 mL solvent mixture of water and ethanol (1:1 in volume) and ultrasonicated for 20 min to obtain an emulsion solution at room temperature. Then, 20 mg TAPB (dissolved in 0.5 mL 0.5 M hydrochloric acid) was slowly added to the solution under vigorous stirring to form a nanoemulsion system. After stirring for 1 h, 0.1 g ammonium persulfate (4.8 wt% in water) was injected into the above mixture and stirred for 12 h continuously to induce the self-polymerization of 1,3,5-Tris(4-aminophenyl) benzene oligomers. The N-doped resin nanospheres were obtained by centrifuging and washing with tetrahydrofuran, deionized water, and ethanol in sequence at least three times. Then, the resulting products were dried at 60  $^{\circ}\text{C}$  for 24 h in an oven.

The N-doped amorphous carbon nanospheres could be easily produced after pyrolyzation of N-doped resin nanospheres by preheating at 350  $^{\circ}\text{C}$  for 3 h and further heating at 800  $^{\circ}\text{C}$  for 2 h with a heating rate of 1  $^{\circ}\text{C min}^{-1}$  under a  $\text{N}_2$  atmosphere.

The surface pore sizes of the carbon nanospheres could be customized by adjusting the amount of toluene in the reaction system. In this work, different volumes of toluene (10  $\mu\text{L}$ , 50  $\mu\text{L}$ , 100  $\mu\text{L}$ , and 200  $\mu\text{L}$ ) were used to form various N-doped resin nanospheres with adjustable pore sizes. After the carbonization, the corresponding N-doped amorphous carbon nanospheres were obtained.

### 2.3. Characterization

TEM was carried out at 200 kV with the JEM 2100Plus (JEOL, Akishima, Japan). SEM analysis was performed using a Zeiss GeminiSEM450 microscope (Jena, Germany). XRD patterns were collected with  $\text{Cu K}\alpha$  radiation (40 kV, 40 mA) by using the Bruker D8 (Karlruhe, Germany). Nitrogen adsorption/desorption isotherms at 77 K were characterized by using a Quantachrome Autosorb-iQ-MP-AG (Boynton Beach, FL, USA). XPS was collected using a Thermo Fisher ESCALAB 250Xi (Shanghai, China) with a monochrome Al source. All the binding energies were modified using the C 1s standard peak at 284.6 eV. Raman spectra were recorded on a microscopic Raman spectrometer (ANDOR SR-500I-D2-1F1 500 mm focal length, motorized Czerny-Turner Spectrograph, UK) (TechnoSpex Pte Ltd., Singapore), using a He-Ne laser with an excitation wavelength of 532 nm.

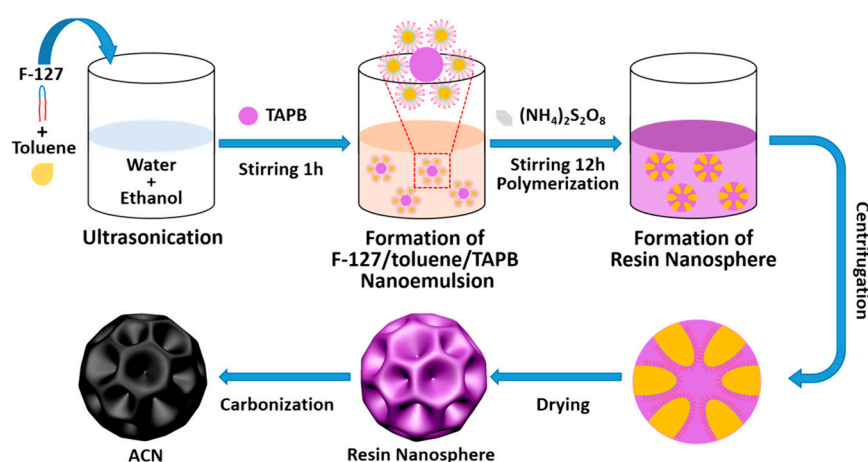
### 2.4. Electrochemical Measurements

The slurry was prepared by mixing 70 wt% of active materials (ACNs-10, ACNs-50, ACNs-100, ACNs-200), 10 wt% of binder (polyvinylidene fluoride, PVDF) in N-Methylpyrrolidone, and 20 wt% of Super P carbon black. The working electrode was prepared by casting the slurry onto copper foil and dried at 60  $^{\circ}\text{C}$  in a vacuum oven for 12 h. The areal mass loading of active materials was  $\sim 0.25 \text{ mg cm}^{-2}$ . The coated copper foil was cut into 12 mm diameter disks. The CR 2032 coin cells were assembled in an Ar-filled glovebox. Lithium metal foil ( $\Phi 15.6 \times 0.45 \text{ mm}$ ) was used as counter electrode and the Celgard 2500 polypropylene membrane was used as separator. A concentration of 1.0 M  $\text{LiPF}_6$  in a 3:7 (v/v) mixture of ethylene carbonate and ethyl methyl carbonate was adopted as the electrolyte. Galvanostatic discharge/charge and rate capacity were operated with a voltage range of 0.01–3 V (vs.  $\text{Li}^+/\text{Li}$ ) on the Neware CT-4008Tn test system (BTS Client 8.0.0.575 version) (Shenzhen, China). Cyclic voltammetry (CV) was evaluated at a scan rate of 0.1  $\text{mV s}^{-1}$  in the voltage window between 0.01 and 3 V with a Bio-Logic VMP3 FlexP

0160 instrumentation system (Seysyine, France). Electrochemical impedance spectroscopy (EIS) was conducted in the frequency range from 0.01 Hz to 100 kHz.

### 3. Results and Discussion

To enhance the safety of the synthesis processes for ACNs, we employed a safe methodology, outlined in Scheme 1. Resin nanospheres with different surface pore sizes were synthesized by multi-purpose nanoemulsion method [33], using 1,3,5-tris (4-aminophenyl) benzene (TAPB) as a carbon source, Pluronic F-127 as a surfactant, and toluene as a soft template. Toluene played a key role in tuning the surface pore size, promoting enhanced hydrophobic interaction between toluene and F-127-derived polypropylene oxide segments [34]. The F-127/toluene/TAPB nanoemulsion in a mixed system of water and ethanol served as the nucleation site of TAPB polymerization during the synthesis process. As the polymerization progressed, the resin nanospheres underwent growth with F-127/toluene/TAPB nanoemulsions adsorbing onto their surface to prevent aggregation. This protective mechanism resulted in the formation of resin nanospheres with ordered porous surfaces [35]. The polymerization with  $(\text{NH}_4)_2\text{S}_2\text{O}_8$  as a catalyst in the complex emulsions further facilitated the fusion of thermodynamically unstable emulsions [33], followed by the removal of toluene to obtain resin nanospheres with different pore sizes. In the final step, these resin nanospheres were subjected to sintering and carbonization processes to produce four distinct types of ACNs, denoted as ACNs-10, ACNs-50, ACNs-100, and ACNs-200, signifying the utilization of 10, 50, 100, and 200  $\mu\text{L}$  of toluene in the synthesis process, respectively.



**Scheme 1.** Schematic of the synthesis procedure of ACNs.

SEM and TEM, as depicted in Figure 1, revealed the unmodified surface morphology of the ACNs-10 with a diameter of  $\sim 400$  nm. In contrast, the diameters of the ACNs-50, ACNs-100, and ACNs-200, featuring surface pore modification, fell within the range of 40–60 nm. The substantial size difference between the ACNs-10 and other samples arose from the inadequacy of 10  $\mu\text{L}$  of toluene used in the synthesis of the ACNs-10 to effectively interact with F-127, preventing the formation of a stable F-127/toluene/TAPB nanoemulsion. Under this condition, toluene and F-127 collaborate to stabilize the resin nanospheres by adjusting the surface amphiphilicity, yielding smooth, large-sized, non-porous resin nanospheres [36]. With the addition of an increased amount of toluene ( $\geq 50$   $\mu\text{L}$ ), a stable F-127/toluene/TAPB nanoemulsion forms, facilitating TAPB polymerization and producing smaller-sized resin nanospheres. The surface porous structure is favorable for electrolyte infiltration and penetration of the anode material, effectively shortening the diffusion length of the lithium ions [37]. Compared to the ACNs-50, both ACNs-100 and ACNs-200 exhibited larger and deeper surface pores, indicating the tunability of the surface pore size of the nanosphere through adjustments to the addition of toluene. In addition, when utilizing 10, 50, and 100  $\mu\text{L}$  of toluene, the resulting emulsions exhibited clarity and trans-

parency. However, with the use of 200  $\mu\text{L}$  of toluene, a turbid mixed liquid was generated (Figure S3). Hence, it can be inferred that excess toluene does not contribute to the formation of the nanoemulsion. This observation may account for the similarity in the size and surface morphology between the ACNs-100 and ACNs-200. Furthermore, in Figure S1, a disordered graphitic structure within the ACNs was observed, displaying predominantly discontinuous graphite-like layers with numerous internal defects. This feature may be beneficial for lithium ion storage, as suggested by previous literature [5].

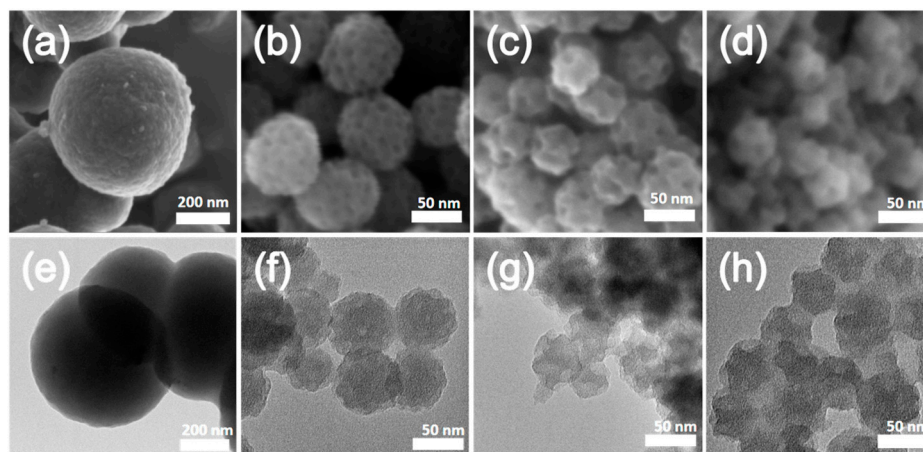


**Figure 1.** SEM images of (a) ACNs-10, (b) ACNs-50, (c) ACNs-100, and (d) ACNs-200, and TEM images of (e) ACNs-10, (f) ACNs-50, (g) ACNs-100, and (h) ACNs-200.

Further XRD characterization revealed the presence of two broad peaks for the ACNs (Figure 2a). Notably, the (002) peak exhibited a substantial reduction in intensity and broadening compared to the XRD pattern of the resin nanospheres before carbonization (Figure S2). This observation emphasized the limited degree of graphitization within the carbon nanospheres, indicating an inherently disordered carbon structure. This was also confirmed by the results of the Raman spectroscopy (Figure 2b), which exhibited two peaks at  $\sim 1350$  and  $\sim 1590$   $\text{cm}^{-1}$ , representing  $\text{sp}^3$  carbon (D band) and  $\text{sp}^2$  carbon (G band), respectively, with a calculated  $I_{\text{D}}/I_{\text{G}}$  ratio of 1.25. It was clearly observed that the intensity of the D band surpasses that of the G band, indicating a significant presence of defects and disordered non-graphitic carbon structures in the nanospheres [38]. The nitrogen adsorption/desorption isotherms are shown in Figure 2c. The specific surface area ( $S_{\text{BET}}$ ) was calculated using the Brunauer–Emmett–Teller model, while the micropore surface area ( $S_{\text{MICRO}}$ ), micropore volume ( $V_{\text{MICRO}}$ ), and external surface area ( $S_{\text{EX}}$ ) were calculated using the t-plot method. The corresponding results are summarized in Table S1. It was evident that the  $S_{\text{BET}}$  and  $S_{\text{MICRO}}$  of the ACNs-10 are significantly smaller and larger, respectively, compared to the other samples. This is primarily attributed to its larger particle size and the absence of surface pore modification. In the case of the pore-modified ACN samples, the ACNs-100 exhibited the highest  $S_{\text{BET}}$ , at  $\sim 618$   $\text{m}^2$   $\text{g}^{-1}$ . As the surface pore size and depth increase, there is a gradual decrease in the  $S_{\text{MICRO}}$  and a corresponding increase in the  $S_{\text{EX}}$ . The similar  $S_{\text{EX}}$  observed in the ACNs-100 and ACNs-200 suggested a potential similarity in surface morphology, which is consistent with the SEM and TEM findings.

The full spectrum (Figure 2d) of the XPS revealed three clear peaks, corresponding to C 1 s, N 1 s, and O 1 s in the ACNs, and, notably, there were no impurities present. The elemental contents of C, N, and O are 89.2, 5.0, and 5.8 wt%, respectively. In the XPS C 1 s spectrum (Figure 2e), three distinct carbon species, namely, C = C, C – N, and O – C = O, can be identified, each exhibiting binding energies of 284.6, 285.9, and 289.4 eV, respectively [34]. In addition, as depicted in Figure 2f, the N 1 s spectrum can be fitted into three discernible peaks: pyridinic N at 398.5 eV, pyrrolic N at 400.9 eV, and graphitic N at 403.6 eV [39,40]. The pyridinic N and pyrrolic N in the ACNs can constitute a lot of

defects and serve as the active site for lithium storage, thus increasing the lithium battery capacity [5,40].

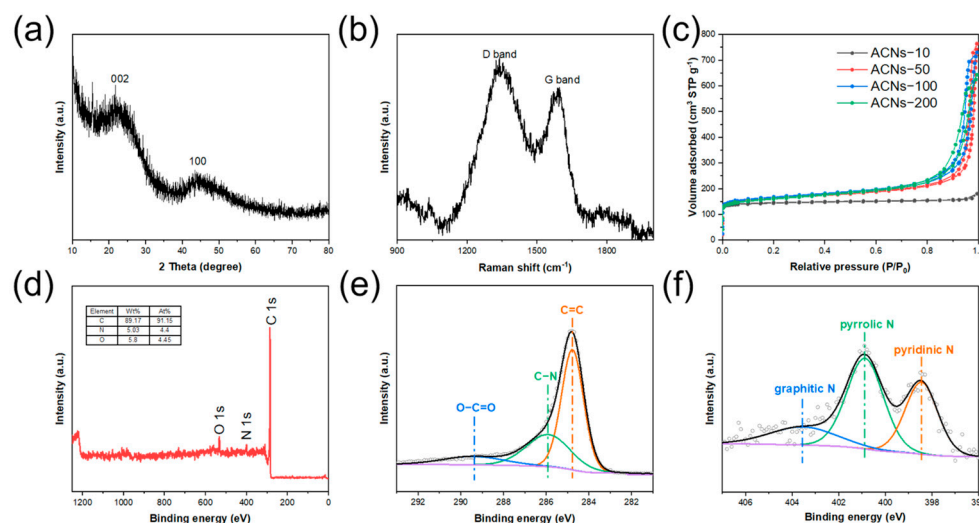


**Figure 2.** (a) XRD pattern of ACNs, (b) Raman spectrum of ACNs, (c) nitrogen adsorption/desorption isotherms of ACNs. (d) XPS full spectrum of ACNs. XPS spectra of (e) C 1s and (f) N 1s.

To evaluate the electrochemical performance of the ACN anode, a Li/ACN lithium-ion half battery was assembled in a button cell, employing thin lithium metal foil as the counter electrode, ACNs as the working electrode, and  $\text{LiPF}_6$  as the electrolyte. At a charging and discharging rate of 0.05 C, the initial discharge (lithiation) capacities of the battery with ACNs-10, ACNs-50, ACNs-100, and ACNs-200 electrodes were 698, 985, 1159, and 1123  $\text{mAh g}^{-1}$ , respectively (Figure 3a). The presence of disordered carbon and a micropore structure within the ACNs contributes to their increased lithium storage capacity and enhanced ion transport channels [24,26]. Simultaneously, surface pore modification adds to the external surface area of the ACNs, facilitating a broader contact area with the electrolyte. This exposure of more active sites serves to reduce ion transport paths, ultimately offering a greater storage capacity for lithium ions [24,27]. In the subsequent rate performance test cycled at different rates from 0.05 C to 25 C, as shown in Figure 3b, the surface-pore-modified ACNs consistently outperformed the unmodified ACNs-10. This enhancement is attributed to their significantly larger external surface area. The ACNs-100 consistently maintained the highest discharge capacity at each rate, with a capacity of approximately  $600 \text{ mAh g}^{-1}$  at a low rate of 0.05 C and  $145 \text{ mAh g}^{-1}$  at a high rate of 25 C. This is attributed to its small size and relatively large specific surface area and external surface area. This characteristic has great potential in fast charging applications. Upon returning to 0.5 C at the end of the rate performance test, the capacity of the Li/ACN batteries showed an increase. The ACNs-200 exhibited a similar capacity to the ACNs-100 at various rates, which corresponds to their morphology being almost identical to that of the ACNs-100.

The charge–discharge curve at a rate of 0.05 C and cyclic voltammetry (CV) curve at a scan rate of  $0.1 \text{ mV s}^{-1}$  of the ACNs-100 battery are shown in Figure 3c,d. In the initial cycle, the specific capacity of discharge (lithiation) and charge (delithiation) were 1159 and  $566 \text{ mAh g}^{-1}$ , respectively, with a Coulombic efficiency of 49%. The considerable irreversible capacity is mainly attributed to the formation of the solid electrolyte interphase (SEI) and the presence of an irreversible active site [41,42]. Furthermore, it was observed that the voltage plateau and redox peak are not well-defined when the battery capacity has stabilized, indicating that the ACNs-100 electrode has multiple lithium storage behaviors. The capacity in the voltage range of 2.0–3.0 V is mainly attributed to the binding of the lithium ions with nitrogen atoms and physical adsorption, while the capacity in the voltage range of 0.8–2.0 V arises from the trapping of lithium ions by the defects in the ACNs-

100 [37,43–45]. The region with a voltage below 0.8 V contributes 75% of the capacity, which is attributed to lithium ion intercalation into the graphite layers, and the voltage slope implies a disordered stacking of the graphite sheets [37,43].

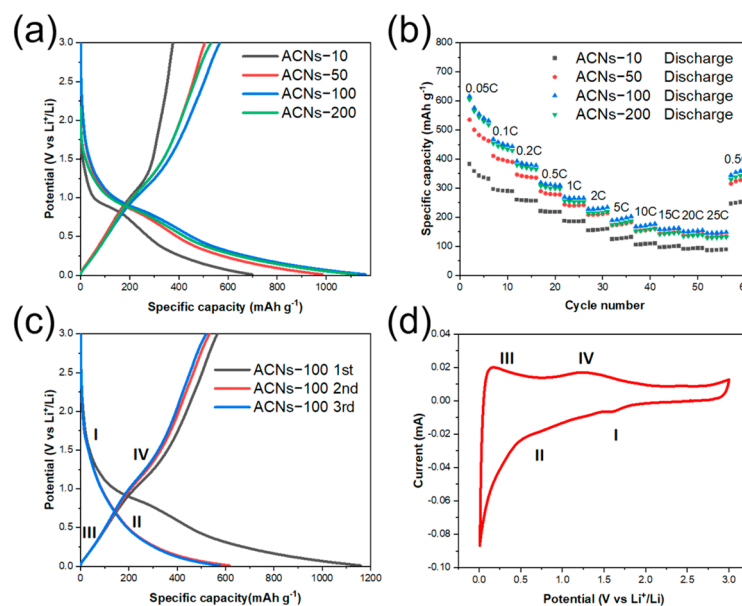


**Figure 3.** Electrochemical characteristics of ACN electrodes: (a) initial galvanostatic charge–discharge curves of ACN electrode at a rate of 0.05 C, (b) rate performance of ACN electrodes, (c) initial three galvanostatic charge–discharge curves of ACNs-100 electrode at a rate of 0.05 C, (d) CV curve of ACNs-100 at a scan rate of  $0.1 \text{ mV s}^{-1}$  (I, II, III, and IV represent the different REDOX reaction stages in the charge-discharge process).

Figure 4 shows the cycling stability test of the Li/ACN batteries at a rate of 2 C for 2000 cycles. Interestingly, the capacity of all the ACN batteries increased with the growing cycle number. ACNs-100 and ACNs-200 achieved their maximum capacities at the ~1100th cycle before experiencing decay, while the ACNs-50 and ACNs-10 maximized their capacities at the ~1300th and ~2000th cycles, respectively. The order of their maximum capacities is ACNs-100 > ACNs-200 > ACNs-50 > ACNs-10, signifying that the surface pore modification of the carbon nanospheres contributes to enhanced battery performance, with a larger surface pore demonstrating superior performance. In the case of the ACNs-100, the specific capacity of the battery initiated from  $320 \text{ mAh g}^{-1}$  and steadily rose, reaching a maximum of  $655 \text{ mAh g}^{-1}$  after ~1100 cycles. The capacity of the ACNs-200 closely paralleled that of the ACNs-100 throughout the entire stability cycling, aligning with their rate performances. The similar morphology, surface area, and battery performance of the ACNs-100 and ACNs-200 suggested that the maximum amount of toluene addition in the synthesis process is approximately  $100 \mu\text{L}$ .

To investigate the persistent capacity increase observed over a thousand cycles, we employed electrochemical impedance spectroscopy (EIS) to gain a deeper understanding of the kinetic behavior of the ACN electrodes, both before cycling and after long-term cycling. As shown in both Nyquist diagrams before and after cycling (Figure 5), using the Li/ACNs-100 battery as an illustrative example, clear sunken semicircles were observed in the middle- and high-frequency region, indicating the presence of charge transfer resistance. The charge transfer resistance for the battery after cycling is less than  $50 \Omega$ , a substantial reduction compared to the pre-cycling resistance of  $\sim 900 \Omega$ . This substantial reduction in charge transfer resistance after cycling is conducive to the implementation of lithium ion transport for storage, providing partial insight into the observed capacity increase in the Li/ACN battery during cycling. This phenomenon of capacity increase, previously reported multiple times [38,40,46], can be attributed to the reciprocal movement of lithium ions

into and out of the graphite-like interlayer structure within the ACNs during charge and discharge cycling, resulting in an expanded spacing between the graphite-like interlayers, consequently creating more room for lithium storage [47]. Another explanation is that the amorphous carbon material broke due to the reciprocating insertion of lithium ions during the charging and discharging process, exposing more active sites and defects [48]. The XRD pattern of the ACNs-100 after cycling (Figure S4) revealed the absence of the original (002) and (100) peaks within the amorphous carbon nanospheres, indicating the complete disordering of the internal structure. It is hypothesized that the repeated lithium ion insertion and removal may disrupt the ordered structure within ACNs, potentially creating additional storage space and, therefore, increased capacity. These conditions allow for more lithium to be embedded in the amorphous carbon in the next cycle, increasing the discharge capacity.

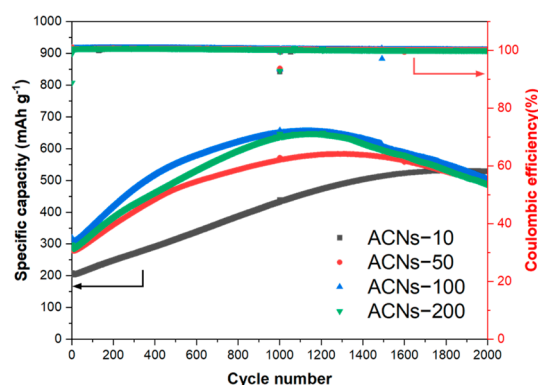


Figure 4. Long-term cycling stability of Li/ACN cells at a rate of 2 C.

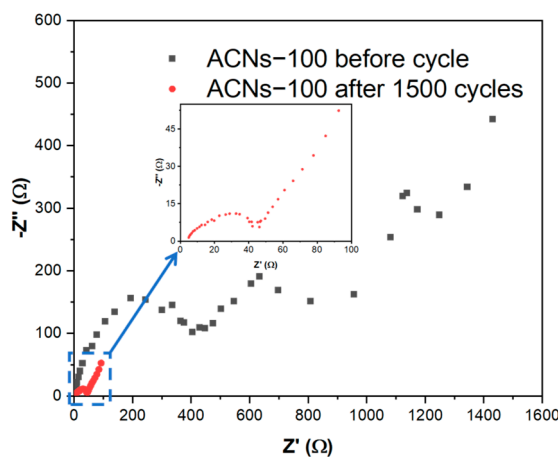


Figure 5. Electrochemical impedance spectra of the Li/ACNs-100 battery before and after cycling.

#### 4. Conclusions

In conclusion, a safe methodology was employed to synthesize ACNs with controlled surface pore modification, achieved through the precise control of toluene addition during the nanoemulsion process. SEM and TEM revealed distinct surface morphologies for various ACNs. XRD and Raman spectroscopy provided insights into their structural characteristics, highlighting the inherently disordered carbon structure of the ACNs. The nitrogen adsorption/desorption isotherms indicated a direct correlation between the external surface area and surface pore modification. The XPS exhibited elemental compositions of C, N, and O in the ACNs. The electrochemical measurements of the initial discharge capacity, rate performance, and cycling stability confirmed the enhanced performance of the surface-pore-modified ACNs, with the ACNs-100 exhibiting the most outstanding results. A persistent rise in capacity was observed in the cycling test, notably in the ACNs-100,

where the specific capacity increased from an initial 320 mAh g<sup>-1</sup> to a peak of 655 mAh g<sup>-1</sup> at a rate of 2 C. This phenomenon was attributed to the reciprocal movement of the lithium ions within the graphite-like interlayer of the ACNs. The EIS provided evidence of reduced charge transfer resistance after cycling, contributing to enhanced lithium-ion transport and storage. The observed improvements in the electrochemical performance underscore the significance of tailored nanostructure engineering in advancing the field of energy storage materials.

**Supplementary Materials:** The following supporting information can be downloaded at <https://www.mdpi.com/article/10.3390/nano14090772/s1>, Figure S1: HR-TEM images of ACNs-100; Figure S2: XRD pattern of resin nanospheres; Figure S3: Images of the resulting F-127/toluene/TAPB nanoemulsions with the addition of 10 µL, 50 µL, 100 µL, and 200 µL toluene; Table S1: Specific surface areas of ACNs; Figure S4: XRD pattern of ACNs-100 after cycling.

**Author Contributions:** S.S., C.Y. and T.-C.W. conceived the idea for the project and designed the experiments. C.Y. and T.-C.W. supervised the project. T.-C.W. searched for funding. S.S. fabricated the ACNs and assembled the batteries. S.S., G.L. and J.Z. conducted the structure characterizations and data analysis. S.S., G.L. and G.T. assisted in electrochemical measurements. T.-C.W., L.L. and C.X. provided some experimental methods. S.S. and C.Y. wrote the manuscript. All authors have read and agreed to the published version of the manuscript.

**Funding:** This research was funded by the National Key Research and Development Program of the Ministry of Science and Technology of China (2021YFA1500604), the National Natural Science Foundation of China financial support (NSFC-21727801), and ShanghaiTech University start-up funding.

**Data Availability Statement:** Data are available on demand.

**Acknowledgments:** We would like to thank the Analytical Instrumentation Center (#SPST-AIC 10112914) at the School of Physical Science and Technology (SPST), ShanghaiTech University, for their generous support. We appreciate the Centre for High-Resolution Electron Microscopy (ChEM), which is supported by SPST of ShanghaiTech University under contract No. EM02161943.

**Conflicts of Interest:** The authors declare that they have no conflicts of interest.

## References

1. Goodenough, J.B.; Kim, Y. Challenges for Rechargeable Li Batteries. *Chem. Mater.* **2010**, *22*, 587–603. [[CrossRef](#)]
2. Tang, W.J.; Wu, J.B.; Wang, X.L.; Xia, X.H.; Tu, J.P. Integrated carbon nanospheres arrays as anode materials for boosted sodium ion storage. *Green Energy Environ.* **2018**, *3*, 50–55. [[CrossRef](#)]
3. Dunn, B.; Kamath, H.; Tarascon, J.M. Electrical Energy Storage for the Grid: A Battery of Choices. *Science* **2011**, *334*, 928–935. [[CrossRef](#)] [[PubMed](#)]
4. Kang, B.; Ceder, G. Battery materials for ultrafast charging and discharging. *Nature* **2009**, *458*, 190–193. [[CrossRef](#)] [[PubMed](#)]
5. Kaskhedikar, N.A.; Maier, J. Lithium Storage ion Carbon Nanostructures. *Adv. Mater.* **2009**, *21*, 2664–2680. [[CrossRef](#)] [[PubMed](#)]
6. Li, H.; Huang, X.J.; Chen, L.Q.; Wu, Z.G.; Liang, Y. A high capacity nano-Si composite anode material for lithium rechargeable batteries. *Electrochem. Solid-State Lett.* **1999**, *2*, 547–549. [[CrossRef](#)]
7. Qian, J.F.; Henderson, W.A.; Xu, W.; Bhattacharya, P.; Engelhard, M.; Borodin, O.; Zhang, J.G. High rate and stable cycling of lithium metal anode. *Nat. Commun.* **2015**, *6*, 6362. [[CrossRef](#)]
8. Li, Q.F.; Bjerrum, N.J. Aluminum as anode for energy storage and conversion: A review. *J. Power Sources* **2002**, *110*, 1–10. [[CrossRef](#)]
9. Zhou, G.M.; Wang, D.W.; Li, F.; Zhang, L.L.; Li, N.; Wu, Z.S.; Wen, L.; Lu, G.Q.; Cheng, H.M. Graphene-Wrapped Fe<sub>3</sub>O<sub>4</sub> Anode Material with Improved Reversible Capacity and Cyclic Stability for Lithium Ion Batteries. *Chem. Mater.* **2010**, *22*, 5306–5313. [[CrossRef](#)]
10. Wu, Z.S.; Ren, W.C.; Xu, L.; Li, F.; Cheng, H.M. Doped Graphene Sheets As Anode Materials with Superhigh Rate and Large Capacity for Lithium Ion Batteries. *ACS Nano* **2011**, *5*, 5463–5471. [[CrossRef](#)]
11. Wu, Y.P.; Rahm, E.; Holze, R. Carbon anode materials for lithium ion batteries. *J. Power Sources* **2003**, *114*, 228–236. [[CrossRef](#)]
12. Wu, Z.S.; Ren, W.C.; Wen, L.; Gao, L.B.; Zhao, J.P.; Chen, Z.P.; Zhou, G.M.; Li, F.; Cheng, H.M. Graphene Anchored with Co<sub>3</sub>O<sub>4</sub> Nanoparticles as Anode of Lithium Ion Batteries with Enhanced Reversible Capacity and Cyclic Performance. *ACS Nano* **2010**, *4*, 3187–3194. [[CrossRef](#)] [[PubMed](#)]
13. Wang, H.L.; Cui, L.F.; Yang, Y.A.; Casalongue, H.S.; Robinson, J.T.; Liang, Y.Y.; Cui, Y.; Dai, H.J. Mn<sub>3</sub>O<sub>4</sub>-Graphene Hybrid as a High-Capacity Anode Material for Lithium Ion Batteries. *J. Am. Chem. Soc.* **2010**, *132*, 13978–13980. [[CrossRef](#)] [[PubMed](#)]

14. Wang, H.Y.; Abe, T.; Maruyama, S.; Iriyama, Y.; Ogumi, Z.; Yoshikawa, K. Graphitized carbon nanobeads with an onion texture as a lithium-ion battery negative electrode for high-rate use. *Adv. Mater.* **2005**, *17*, 2857–2860. [[CrossRef](#)]
15. Su, F.B.; Zhao, X.S.; Wang, Y.; Wang, L.K.; Lee, J.Y. Hollow carbon spheres with a controllable shell structure. *J. Mater. Chem.* **2006**, *16*, 4413–4419. [[CrossRef](#)]
16. Yan, X.D.; Teng, D.H.; Jia, X.L.; Yu, Y.H.; Yang, X.P. Improving the cyclability and rate capability of carbon nanofiber anodes through in-site generation of SiO<sub>x</sub>-rich overlayers. *Electrochim. Acta* **2013**, *108*, 196–202. [[CrossRef](#)]
17. Tang, J.J.; Chen, G.H.; Yang, J.; Zhou, X.Y.; Zhou, L.N.; Huang, B. Silica-assistant synthesis of three-dimensional graphene architecture and its application as anode material for lithium ion batteries. *Nano Energy* **2014**, *8*, 62–70. [[CrossRef](#)]
18. Zhan, Y.F.; Zhang, B.D.; Cao, L.M.; Wu, X.X.; Lin, Z.P.; Yu, X.; Zhang, X.X.; Zeng, D.R.; Xie, F.Y.; Zhang, W.H.; et al. Iodine doped graphene as anode material for lithium ion battery. *Carbon* **2015**, *94*, 1–8. [[CrossRef](#)]
19. Zhang, J.; Hu, Y.S.; Tessonnier, J.P.; Weinberg, G.; Maier, J.; Schlogl, R.; Su, D.S. CNFs@CNTs: Superior carbon for electrochemical energy storage. *Adv. Mater.* **2008**, *20*, 1450–1455. [[CrossRef](#)]
20. Cheng, X.; Tang, C.; Yan, C.; Du, J.; Chen, A.; Liu, X.; Jewell, L.; Zhang, Q. Preparation of porous carbon spheres and their application as anode materials for lithium-ion batteries: A review. *Mater. Today Nano* **2023**, *22*, 100321. [[CrossRef](#)]
21. Bi, J.X.; Du, Z.Z.; Sun, J.M.; Liu, Y.H.; Wang, K.; Du, H.F.; Ai, W.; Huang, W. On the Road to the Frontiers of Lithium-Ion Batteries: A Review and Outlook of Graphene Anodes. *Adv. Mater.* **2023**, *35*, e2210734. [[CrossRef](#)] [[PubMed](#)]
22. Li, Y.; Wu, F.F.; Jin, X.; Xu, H.M.; Liu, X.F.; Shi, G. Preparation and electrochemical properties of graphene quantum dots/biomass activated carbon electrodes. *Inorg. Chem. Commun.* **2020**, *112*, 107718. [[CrossRef](#)]
23. Roberts, A.D.; Li, X.; Zhang, H.F. Porous carbon spheres and monoliths: Morphology control, pore size tuning and their applications as Li-ion battery anode materials. *Chem. Soc. Rev.* **2014**, *43*, 4341–4356. [[CrossRef](#)] [[PubMed](#)]
24. Etacheri, V.; Wang, C.W.; O’Connell, M.J.; Chan, C.K.; Pol, V.G. Porous carbon sphere anodes for enhanced lithium-ion storage. *J. Mater. Chem. A* **2015**, *3*, 9861–9868. [[CrossRef](#)]
25. Liu, J.; Qiao, S.Z.; Liu, H.; Chen, J.; Orpe, A.; Zhao, D.Y.; Lu, G.Q. Extension of The Stober Method to the Preparation of Monodisperse Resorcinol-Formaldehyde Resin Polymer and Carbon Spheres. *Angew. Chem. Int. Ed.* **2011**, *50*, 5947–5951. [[CrossRef](#)] [[PubMed](#)]
26. Wang, G.; Sun, Y.H.; Li, D.B.; Liang, H.W.; Dong, R.H.; Feng, X.L.; Mullen, K. Controlled Synthesis of N-Doped Carbon Nanospheres with Tailored Mesopores through Self-Assembly of Colloidal Silica. *Angew. Chem. Int. Ed.* **2015**, *54*, 15191–15196. [[CrossRef](#)] [[PubMed](#)]
27. Chang, P.Y.; Bindumadhavan, K.; Doong, R.A. Size Effect of Ordered Mesoporous Carbon Nanospheres for Anodes in Li-Ion Battery. *Nanomaterials* **2015**, *5*, 2348–2358. [[CrossRef](#)] [[PubMed](#)]
28. Paraknowitsch, J.P.; Thomas, A. Doping carbons beyond nitrogen: An overview of advanced heteroatom doped carbons with boron, sulphur and phosphorus for energy applications. *Energy Environ. Sci.* **2013**, *6*, 2839–2855. [[CrossRef](#)]
29. Ni, W.; Shi, L.Y. Review Article: Layer-structured carbonaceous materials for advanced Li-ion and Na-ion batteries: Beyond graphene. *J. Vac. Sci. Technol. A* **2019**, *37*, 040803. [[CrossRef](#)]
30. Wang, X.; Weng, Q.H.; Liu, X.Z.; Wang, X.B.; Tang, D.M.; Tian, W.; Zhang, C.; Yi, W.; Liu, D.Q.; Bando, Y.; et al. Atomistic Origins of High Rate Capability and Capacity of N-Doped Graphene for Lithium Storage. *Nano Lett.* **2014**, *14*, 1164–1171. [[CrossRef](#)]
31. Lin, Q.W.; Zhang, J.; Lv, W.; Ma, J.B.; He, Y.B.; Kong, F.Y.; Yang, Q.H. A Functionalized Carbon Surface for High-Performance Sodium-Ion Storage. *Small* **2020**, *16*, e1902603. [[CrossRef](#)] [[PubMed](#)]
32. Zheng, F.C.; Yang, Y.; Chen, Q.W. High lithium anodic performance of highly nitrogen-doped porous carbon prepared from a metal-organic framework. *Nat. Commun.* **2014**, *5*, 5261. [[CrossRef](#)] [[PubMed](#)]
33. Shi, L.M.; Li, W.D.; Wu, Y.; Wei, F.C.; Zhang, T.T.; Fu, J.W.; Jing, C.B.; Cheng, J.G.; Liu, S.H. Controlled Synthesis of Mesoporous pi-Conjugated Polymer Nanoarchitectures as Anodes for Lithium-Ion Batteries. *Macromol. Rapid Commun.* **2022**, *43*, 2100897. [[CrossRef](#)] [[PubMed](#)]
34. Guan, B.Y.; Yu, L.; Lou, X.W. Formation of Asymmetric Bowl-Like Mesoporous Particles via Emulsion-Induced Interface Anisotropic Assembly. *J. Am. Chem. Soc.* **2016**, *138*, 11306–11311. [[CrossRef](#)] [[PubMed](#)]
35. Yang, X.Y.; Lu, P.H.; Yu, L.; Pan, P.P.; Elzatahry, A.A.; Alghamdi, A.; Luo, W.; Cheng, X.W.; Deng, Y.H. An Efficient Emulsion-Induced Interface Assembly Approach for Rational Synthesis of Mesoporous Carbon Spheres with Versatile Architectures. *Adv. Funct. Mater.* **2020**, *30*, 202002488. [[CrossRef](#)]
36. Peng, L.; Hung, C.T.; Wang, S.W.; Zhang, X.M.; Zhu, X.H.; Zhao, Z.W.; Wang, C.Y.; Tang, Y.; Li, W.; Zhao, D.Y. Versatile Nanoemulsion Assembly Approach to Synthesize Functional Mesoporous Carbon Nanospheres with Tunable Pore Sizes and Architectures. *J. Am. Chem. Soc.* **2019**, *141*, 7073–7080. [[CrossRef](#)]
37. Wang, Z.L.; Xu, D.; Wang, H.G.; Wu, Z.; Zhang, X.B. In Situ Fabrication of Porous Graphene Electrodes for High-Performance Energy Storage. *ACS Nano* **2013**, *7*, 2422–2430. [[CrossRef](#)]
38. Qie, L.; Chen, W.M.; Wang, Z.H.; Shao, Q.G.; Li, X.; Yuan, L.X.; Hu, X.L.; Zhang, W.X.; Huang, Y.H. Nitrogen-Doped Porous Carbon Nanofiber Webs as Anodes for Lithium Ion Batteries with a Superhigh Capacity and Rate Capability. *Adv. Mater.* **2012**, *24*, 2047–2050. [[CrossRef](#)] [[PubMed](#)]
39. Zhong, M.; Kim, E.K.; McGann, J.P.; Chun, S.E.; Whitacre, J.F.; Jaroniec, M.; Matyjaszewski, K.; Kowalewski, T. Electrochemically Active Nitrogen-Enriched Nanocarbons with Well-Defined Morphology Synthesized by Pyrolysis of Self-Assembled Block Copolymer. *J. Am. Chem. Soc.* **2012**, *134*, 14846–14857. [[CrossRef](#)]

40. Song, H.W.; Li, N.; Cui, H.; Wang, C.X. Enhanced storage capability and kinetic processes by pores- and hetero-atoms- riched carbon nanobubbles for lithium-ion and sodium-ion batteries anodes. *Nano Energy* **2014**, *4*, 81–87. [[CrossRef](#)]
41. Chen, Y.M.; Li, X.Y.; Zhou, X.Y.; Yao, H.M.; Huang, H.T.; Mai, Y.W.; Zhou, L.M. Hollow-tunneled graphitic carbon nanofibers through Ni-diffusion-induced graphitization as high-performance anode materials. *Energy Environ Sci.* **2014**, *7*, 2689–2696. [[CrossRef](#)]
42. Zhou, X.Y.; Tang, J.J.; Yang, J.; Xie, J.; Huang, B. Seaweed-like porous carbon from the decomposition of polypyrrole nanowires for application in lithium ion batteries. *J. Mater. Chem. A* **2013**, *1*, 5037–5044. [[CrossRef](#)]
43. Hu, C.G.; Wang, L.X.; Zhao, Y.; Ye, M.H.; Chen, Q.; Feng, Z.H.; Qu, L.T. Designing nitrogen-enriched echinus-like carbon capsules for highly efficient oxygen reduction reaction and lithium ion storage. *Nanoscale* **2014**, *6*, 8002–8009. [[CrossRef](#)] [[PubMed](#)]
44. Yang, G.J.; Li, X.Y.; Guan, Z.R.X.; Tong, Y.X.; Xu, B.; Wang, X.F.; Wang, Z.X.; Chen, L.Q. Insights into Lithium and Sodium Storage in Porous Carbon. *Nano Lett.* **2020**, *20*, 3836–3843. [[CrossRef](#)]
45. Kim, H.; Hyun, J.C.; Kim, D.; Kwak, J.H.; Lee, J.B.; Moon, J.H.; Choi, J.; Lim, H.D.; Yang, S.J.; Jin, H.M.; et al. Revisiting Lithium- and Sodium-Ion Storage in Hard Carbon Anodes. *Adv. Mater.* **2023**, *35*, e2209128. [[CrossRef](#)] [[PubMed](#)]
46. Li, X.N.; Zhu, X.; Zhu, Y.C.; Yuan, Z.Q.; Si, L.L.; Qian, Y.T. Porous nitrogen-doped carbon vegetable-sponges with enhanced lithium storage performance. *Carbon* **2014**, *69*, 515–524. [[CrossRef](#)]
47. Liu, Y.; Yan, X.D.; Yu, Y.H.; Yang, X.P. Self-improving anodes for lithium-ion batteries: Continuous interlamellar spacing expansion induced capacity increase in polydopamine-derived nitrogen-doped carbon tubes during cycling. *J. Mater. Chem. A* **2015**, *3*, 20880–20885. [[CrossRef](#)]
48. Jiang, J.; Zhu, J.H.; Ai, W.; Fan, Z.X.; Shen, X.N.; Zou, C.J.; Liu, J.P.; Zhang, H.; Yu, T. Evolution of disposable bamboo chopsticks into uniform carbon fibers: A smart strategy to fabricate sustainable anodes for Li-ion batteries. *Energy Environ Sci.* **2014**, *7*, 2670–2679. [[CrossRef](#)]

**Disclaimer/Publisher’s Note:** The statements, opinions and data contained in all publications are solely those of the individual author(s) and contributor(s) and not of MDPI and/or the editor(s). MDPI and/or the editor(s) disclaim responsibility for any injury to people or property resulting from any ideas, methods, instructions or products referred to in the content.